

37. M. Halic *et al.*, *Science* **312**, 745 (2006).
 38. K. Mitra *et al.*, *Nature* **438**, 318 (2005).
 39. J. R. Jagath, M. V. Rodnina, W. Wintermeyer, *J. Mol. Biol.* **295**, 745 (2000).
 40. B. Weiche *et al.*, *J. Mol. Biol.* **377**, 761 (2008).
 41. Single-letter abbreviations for the amino acid residues are as follows: A, Ala; G, Gly; Q, Gln; and R, Arg.
 42. We thank K. Zhou for excellent technical assistance and help with crystal preparation during the early stages of the project. Initial crystallographic analysis was performed at beamline 8.2.2 at the Advanced Light Source (ALS), Lawrence Berkeley National Laboratory; we acknowledge C. Ralston for outstanding technical assistance at the ALS. Crystallographic data were

collected at the beamline X06SA at the Swiss Light Source (SLS). We thank A. Brunger for the prerelease version of CNS and for helpful comments on the refinement, C. Schulze-Bries and T. Tomizaki for their outstanding support at the SLS, T. Maier and S. Klinge for critical discussion and reading of the manuscript, and T. Maier and M. Leibundgut for help and assistance with data collection and solving the structure. S.F.A. was funded initially by the Howard Hughes Medical Institute and currently by an ETH postdoctoral fellowship, N.S. is funded by Boehringer Ingelheim Fonds, and K.S. is funded by NIH grant GM078024 to S.S. This work was supported in part by the Howard Hughes Medical Institute (J.A.D.) and by the Swiss National Science Foundation

(SNSF) and the National Center of Excellence in Research (NCCR) Structural Biology program of the SNSF. Atomic coordinates and structure factors for the SRP:SR crystal structure have been deposited with the Protein Data Bank under accession code 2xxa.

Supporting Online Material

www.sciencemag.org/cgi/content/full/331/6019/881/DC1
 Materials and Methods
 Figs. S1 to S8
 Tables S1 and S2
 References

13 August 2010; accepted 18 January 2011
 10.1126/science.1196473

REPORTS

Metallic and Insulating Oxide Interfaces Controlled by Electronic Correlations

H. W. Jang,¹ D. A. Felker,² C. W. Bark,¹ Y. Wang,³ M. K. Niranjan,³ C. T. Nelson,⁴ Y. Zhang,^{4,5} D. Su,⁶ C. M. Folkman,¹ S. H. Baek,¹ S. Lee,¹ K. Janicka,³ Y. Zhu,⁶ X. Q. Pan,⁴ D. D. Fong,⁷ E. Y. Tsymbal,³ M. S. Rzchowski,² C. B. Eom^{1*}

The formation of two-dimensional electron gases (2DEGs) at complex oxide interfaces is directly influenced by the oxide electronic properties. We investigated how local electron correlations control the 2DEG by inserting a single atomic layer of a rare-earth oxide (RO) [*R* is lanthanum (La), praseodymium (Pr), neodymium (Nd), samarium (Sm), or yttrium (Y)] into an epitaxial strontium titanate oxide (SrTiO₃) matrix using pulsed-laser deposition with atomic layer control. We find that structures with La, Pr, and Nd ions result in conducting 2DEGs at the inserted layer, whereas the structures with Sm or Y ions are insulating. Our local spectroscopic and theoretical results indicate that the interfacial conductivity is dependent on electronic correlations that decay spatially into the SrTiO₃ matrix. Such correlation effects can lead to new functionalities in designed heterostructures.

Advanced deposition techniques enable the growth of epitaxial heterostructures with atomically controlled interfaces such as multilayers (1), superlattices (2–4), and ultrathin films (5, 6). In these artificial structures, the interfaces play a prominent role in determining the functionalities of the structures and their applications (7). A recent example is the discovery of two-dimensional electron gases (2DEGs) at the interface between complex insulating oxides (8) such as LaAlO₃/SrTiO₃ (9, 10), LaTiO₃/SrTiO₃ (2), and LaVO₃/SrTiO₃ (11) heterostructures, in

which the 2DEG is confined near the LaO/TiO₂ interface. Magnetic and superconducting ground states of the 2DEG have been identified (12–14),

and applications to field-effect transistors and tunnel junctions have been demonstrated (15–17).

Theoretical work on LaTiO₃/SrTiO₃ superlattices (18) suggests that for a several-unit-cell-thick LaTiO₃ layer, the LaTiO₃/SrTiO₃ interface region is metallic; however, nonmetallic behavior dominates in the LaTiO₃ region away from the interface, resulting from strong electron correlations similar to those found in bulk LaTiO₃. In other bulk rare-earth titanates, the effect of electron correlations depends critically on the rare-earth ion (19). We used the unique electronic character of oxide interfaces, and atomic level control of their structure and composition, to deliberately manipulate the 2DEG electronic properties.

We studied the effect of strong electron correlations on an oxide 2DEG by inserting a single atomic layer of RO (*R* is La, Pr, Nd, Sm, or Y) into an epitaxial SrTiO₃ matrix using pulsed-laser deposition with atomic layer control. The RO layer donates electrons to the conduction band of SrTiO₃. These electrons remain near the inserted RO layer due to Coulomb attraction. We find that the transport properties of these electrons range from metallic to insulating, depending critically

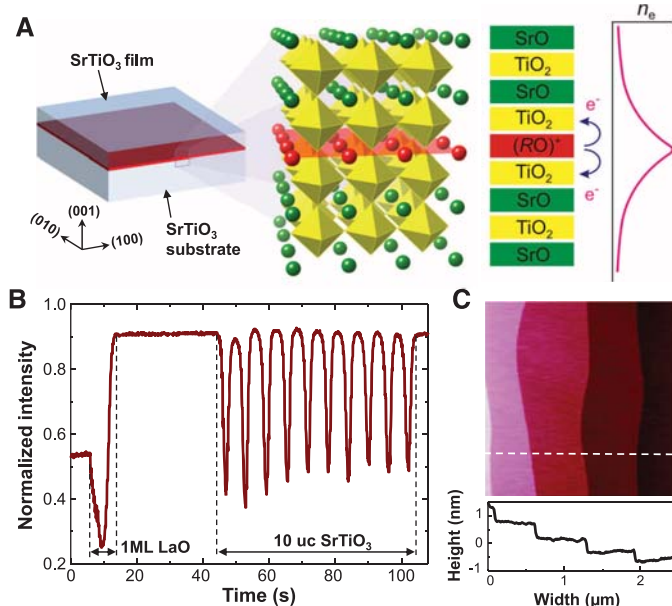


Fig. 1. (A) Schematic representation of a SrTiO₃/1-ML RO/SrTiO₃ heterostructure. The atomic structure near the interface is enlarged. The +1 valent RO layer donates electrons to neighboring TiO₂ planes, leading to the larger electron density n_e near the interface. (B) Typical RHEED oscillations for the growth of 1-ML LaO and 10-uc SrTiO₃ layers in sequence on a TiO₂-terminated SrTiO₃ substrate. (C) AFM image of a 10-uc SrTiO₃/1-ML LaO/SrTiO₃ heterostructure showing an atomically smooth surface.

¹Department of Materials Science and Engineering, University of Wisconsin–Madison, Madison, WI 53706, USA. ²Department of Physics, University of Wisconsin–Madison, Madison, WI 53706, USA. ³Department of Physics and Astronomy, Nebraska Center for Materials and Nanoscience, University of Nebraska–Lincoln, Lincoln, NE 68588, USA. ⁴Department of Materials Science and Engineering, University of Michigan–Ann Arbor, Ann Arbor, MI 48109, USA. ⁵National Laboratory of Solid State Microstructures and Department of Materials Science and Engineering, Nanjing University, Nanjing 210093, P.R. China. ⁶Center for Functional Nanomaterials, Brookhaven National Laboratory, Upton, NY 11973, USA. ⁷Materials Science Division, Argonne National Laboratory, Argonne, IL 60439, USA.

*To whom correspondence should be addressed. E-mail: eom@engr.wisc.edu.

on the rare-earth ion, and that this dependence arises from strong electronic correlations.

We grew epitaxial SrTiO_3 heterostructures containing a symmetric $\text{TiO}_2/\text{RO}/\text{TiO}_2$ interface (Fig. 1A), resulting in RTiO_3 -like structure at the interface. Using pulsed-laser deposition, the heterostructures were fabricated by depositing either a RO monolayer or a RTiO_3 unit cell

on a TiO_2 -terminated SrTiO_3 substrate, followed by deposition of a SrTiO_3 overlayer of varying thickness (20). A thick SrTiO_3 overlayer approximates a single RO monolayer embedded in an infinite SrTiO_3 matrix. Thicknesses of inserted 1-monolayer (ML)-thick RO and 1-unit-cell (uc)-thick RTiO_3 layers were accurately controlled by monitoring in situ reflection high-energy elec-

tron diffraction (RHEED) intensity oscillations. Typical RHEED oscillations for the growth of a 10-uc SrTiO_3 /1-ML LaO heterostructure on a SrTiO_3 substrate are shown in Fig. 1B. The atomic force microscopy (AFM) image of the surface of a complete heterostructure (Fig. 1C) shows the steps and terraces of the original substrate surface, indicating high-quality growth. Microstructure and electrical properties of both SrTiO_3 /1-ML RO/ SrTiO_3 and SrTiO_3 /1-uc RTiO_3 / SrTiO_3 heterostructures were almost identical (20). Here, we focus on the SrTiO_3 /RO/ SrTiO_3 heterostructures.

We first characterized the dependence of electrical properties on growth conditions, using the LaO-based heterostructure, and established the growth conditions of oxygen pressure ($P_{\text{O}_2} = 10^{-3}$ mbar) and temperature ($T_{\text{growth}} = 550^\circ\text{C}$) as optimal (20). These growth conditions were used to fabricate SrTiO_3 heterostructures with single inserted atomic layers of LaO, PrO, NdO, SmO, and YO. Fig. 2A shows the mobile sheet carrier concentration n_s for the five different RO layers as a function of the SrTiO_3 overlayer thickness. It is seen that LaO-, PrO-, and NdO-based heterostructures become conducting above the critical thickness of SrTiO_3 of three or four unit cells. However, SmO- and YO-based heterostructures are insulating, even with a SrTiO_3 overlayer thickness of 100 uc. This is summarized in Fig. 2B, which shows the mobile sheet carrier concentration at fixed overlayer thickness as the rare-earth ion progresses from La to Y. The nominal room-temperature concentration of mobile carriers in crossover NdO-based heterostructures decreases dramatically at lower temperatures (fig. S3D), in contrast to the relatively temperature-independent behavior of the conducting LaO-based and PrO-based heterostructures. This trend is analogous to that in bulk RTiO_3 , where the effects of electron correlations increase as R is varied from La to Y (21). The mobilities of all conducting heterostructures are roughly independent of the rare-earth ion, showing a crossover from temperature-dependent phonon scattering at high temperature to a temperature-independent value at low temperatures.

Our transport measurements are sensitive to mobile carriers near the interface. We also investigated charge transfer from the RO layer to nearby Ti states with electron energy-loss spectroscopy (EELS), sensitive to both mobile and nonmobile carriers (2, 10). For a conducting LaO-based heterostructure, the spatial dependence of EELS spectra of Ti- $L_{2,3}$ and O-K edges is shown in Fig. 3B. The EELS spectra are spatially separated by 0.28 nm, in a line scan across the interface of a 10-uc SrTiO_3 /1-ML LaO/ SrTiO_3 heterostructure (Fig. 3A). Four clear peaks in the Ti $L_{2,3}$ edge become broader at the interface, with peak separations less pronounced. We attribute this broadening to the presence of a Ti^{3+} component. Compared with previous reports (2, 10), the relatively small modulation of the EELS signal at the interface may be related to the low n_s determined from the Hall effect. Our depth profil-

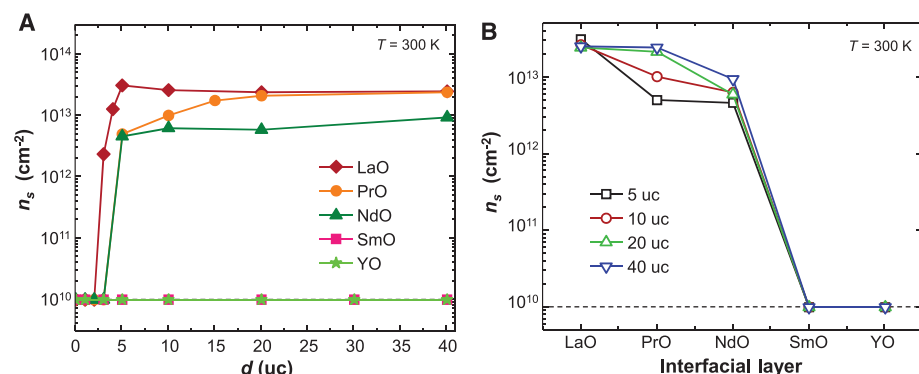


Fig. 2. Dependence of sheet carrier concentration n_s on the R ion in SrTiO_3 /1-ML RO/ SrTiO_3 heterostructures and the SrTiO_3 overlayer thickness d . Sheet carrier concentration is plotted as a function of (A) the thickness of the SrTiO_3 overlayer and (B) the RO doping layer for SrTiO_3 /1-ML RO/ SrTiO_3 heterostructures. SmO-based and YO-based heterostructures never become conducting, even with very thick SrTiO_3 overlayers.

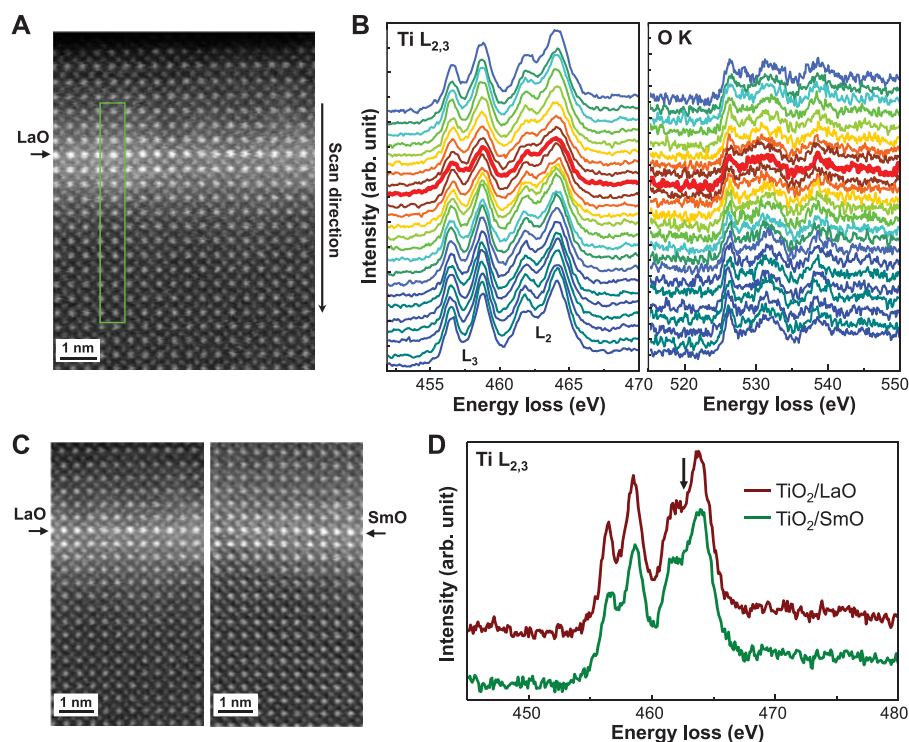


Fig. 3. STEM and EELS analysis. (A) High-angle annular dark field (HAADF) image of a 10-uc SrTiO_3 /1-ML LaO film grown on SrTiO_3 . The rectangular box represents the region of EELS line scans. (B) EELS spectra of Ti- $L_{2,3}$ and O-K edges obtained from 2D line scans across the interface shown in (A). The spacing along the line scan between consecutive EELS spectra is 2.8 Å. The spectra at the LaO layer are highlighted by thicker lines. For the spectra for Ti L_2 and L_3 edges, peak broadening and less pronounced peak splitting at the interface are clearly observed. (C) HAADF images of 10-uc SrTiO_3 /1-ML LaO/ SrTiO_3 and 10-uc SrTiO_3 /1-ML SmO/ SrTiO_3 heterostructures. Both samples show no obvious defects or dislocations, indicating coherent interfaces. (D) Selected area Ti- $L_{2,3}$ EELS spectra obtained at the interfaces for 10-uc SrTiO_3 /1-ML LaO/ SrTiO_3 and 10-uc SrTiO_3 /1-ML SmO/ SrTiO_3 heterostructures. The arrow is a guide for comparison.

ing of the Ti^{3+} to Ti^{4+} ratios indicates that the carriers are confined to within ~ 1 nm of the interface (fig. S6), in good agreement with recent theoretical calculations (22).

Fig. 3, C and D, show scanning transmission electron microscope (STEM) images and selected area $\text{Ti-L}_{2,3}$ EELS spectra, at TiO_2 planes adjacent to the interface, for LaO (conducting) and SmO (insulating) heterostructures. For both heterostructures, the STEM images and the $\text{Ti-L}_{2,3}$ spectra at the interface look very similar. In particular, the very similar peak splittings at ~ 462 eV in the Ti L_2 edges suggest that the electron transfer from the RO layer to the neighboring TiO_2 planes is the same for both LaO- and SmO-based heterostructures. Our transport measurements indicate that these electrons produce a conducting 2DEG in LaO heterostructures but are not mobile in SmO heterostructures.

TiO_6 octahedra rotations in bulk RTiO_3 determine the width of the Ti-3d band of t_{2g} symmetry, and hence the electronic properties, through a change in the Mott-Hubbard gap (23). SrTiO_3 , however, has no TiO_6 octahedral rotations at room temperature. We investigated octahedral rotations in our $\text{SrTiO}_3/\text{RO}/\text{SrTiO}_3$ heterostructures, with synchrotron x-ray experiments at the Advanced Photon Source. We observed strong superlattice reflections (figs. S7 and S8) resulting from unit-cell doubling TiO_6 octahedra rotations, in good agreement with the density functional calculations discussed below. The octahedral rotations are well ordered in the interfacial plane, with typical rocking widths giving an in-plane domain size > 60 nm. The breadths of the half-order peaks in the out-of-plane direction are consistent with octahedral rotations at the RTiO_3 layer rapidly decaying into the SrTiO_3 matrix. These decaying octahedra rotations lead to a spatial gradient in the electronic structure, influencing the conduction.

In addition, epitaxial strain in the interfacial RTiO_3 layer also affects the interface conductivity.

LaTiO_3 , PrTiO_3 , and NdTiO_3 layers at the interface are strained under biaxial compression, but SmTiO_3 and YTiO_3 layers are under biaxial tension (table S1) (21). Compressive strain has been shown to induce conducting behavior in LaTiO_3 thin films (24), attributed to an increased $\text{Ti } t_{2g}$ bandwidth and a weakened crystal field. This has been predicted theoretically to reduce the effect of electron correlations and to support metallic behavior (25). The tensile strain in the SmTiO_3 and YTiO_3 layers embedded in SrTiO_3 appears to enforce the effect of strong correlations and favor insulating behavior.

To understand the combined effects of charge transfer, spatially varying octahedral rotations, biaxial strain, and rare-earth electronic structure, we have performed density functional theory (DFT) calculations, including a Hubbard U term accounting for the on-site Coulomb interaction (20). The values of U that provide a realistic description of the electronic and atomic structure of bulk YTiO_3 and LaTiO_3 compounds (26) were used. The atomic positions were fully relaxed, under the constraint that the in-plane lattice constant be equal to the calculated lattice constant of bulk SrTiO_3 . The density of electronic states, and the corresponding atomic coordinates, calculated for periodic superlattices, are shown in Fig. 4A ($3.5\text{-uc SrTiO}_3/1\text{-ML LaO}$) and in Fig. 4B ($3.5\text{-uc SrTiO}_3/1\text{-ML YO}$). For the LaO-based heterostructure, the Fermi energy lies in the region of nonzero density of states, consistent with the previous calculations (27, 28), whereas for the YO heterostructure the Fermi energy lies between the split-off lower Hubbard band and the higher energy density of states. This indicates that the LaO-based interface is metallic, whereas the YO-based interface is insulating, supporting our experimental observations. Our calculations predict that the ground state of the $\text{SrTiO}_3/\text{LaO}$ heterostructure is not charge-ordered, whereas the SrTiO_3/YO heterostructure

is unstable with respect to charge disproportionation and has a charge-ordered ground state similar to that found in (29). Octahedra rotations are clearly visible in the relaxed structures shown in Fig. 4, C and D, consistent with our synchrotron measurements.

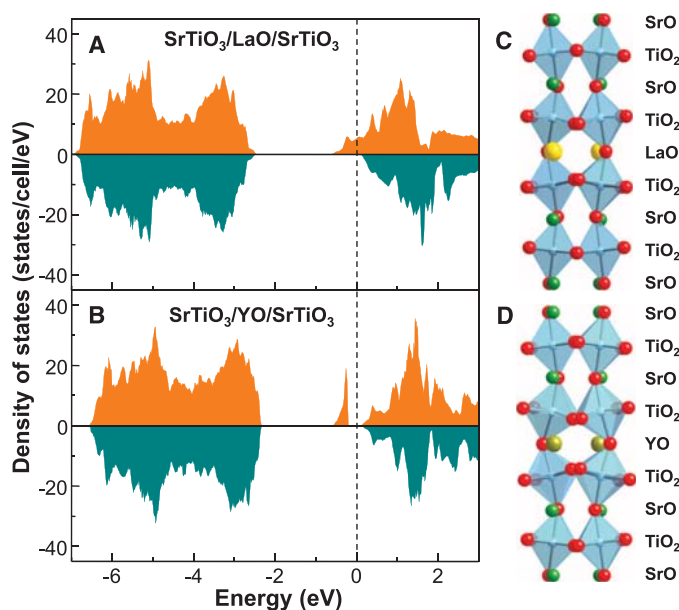
The electron donated by the RO embedded in the SrTiO_3 matrix is localized to the nearby TiO_2 layers. Filling of the Ti-3d band in these layers close to $n = 0.5$, and enhanced electron-correlation effects due to 2D confinement, will strongly influence the interfacial conductivity. It is well known that the effect of Ti-3d band filling on electronic, magnetic, and transport properties of bulk RTiO_3 Mott-Hubbard insulators depends critically on the rare-earth ion (23). It appears that for the relatively weakly correlated LaO-based heterostructure, several percent of hole doping is sufficient to cause a metal-insulator transition. In contrast, for the YO-based heterostructures with larger U , lower bandwidth W , and larger strain and structural distortions, the insulating phase persists. The number of electrons transferred in each case is the same, but stronger correlation effects in the YO heterostructure seem to be responsible for the insulating behavior. Our experimental and theoretical investigations suggest that these correlations arise from an interplay of strain, spatially varying rotational distortions, and rare-earth ion effects on the band structure. Indications of electron correlations have also been recently reported in $\text{LaO}_3/\text{SrTiO}_3$ heterostructures (30).

Strong correlations in 2DEGs at oxide interfaces have been shown to result from electronic properties of different RO inserted layers, as well as the structural and electronic modification of nearby layers. Quantitatively exploring the underlying physics of the experimental data presented here is complex and challenging, because strong correlations combined with atomic-scale structural and chemical variations severely limit the effectiveness of theoretical calculations. The details cannot be fully captured within the DFT+ U calculations used here, and more advanced approaches—based on dynamical mean-field theory (31), for example—are likely necessary to capture the spatial variations. The work presented here is important in elucidating correlation effects in systems with atomic-scale perturbations (32) and external perturbation-induced changes in oxide 2DEG systems (8, 15–17). The ability to design and grow heterostructures with atomic-scale variations, and the demonstrated strong dependence of correlated 2DEGs on these variations, open new directions for oxide 2DEG heterostructures.

References and Notes

1. H. Yamada *et al.*, *Science* **305**, 646 (2004).
2. A. Ohtomo, D. A. Muller, J. L. Grazul, H. Y. Hwang, *Nature* **419**, 378 (2002).
3. M. P. Warusawithana, E. V. Colla, J. N. Eckstein, M. B. Weissman, *Phys. Rev. Lett.* **90**, 036802 (2003).
4. E. Bousquet *et al.*, *Nature* **452**, 732 (2008).
5. M. P. Warusawithana *et al.*, *Science* **324**, 367 (2009).

Fig. 4. Energy-dependent density of states and structural relaxation of $3.5\text{-uc SrTiO}_3/1\text{-ML LaO}$ (A and C) periodic superlattice and $3.5\text{-uc SrTiO}_3/1\text{-ML YO}$ periodic superlattice (B and D) obtained from DFT calculations. Positive density of states is for spin up and negative is for spin down. The dashed line indicates the position of the Fermi level. The results indicate conducting behavior for the $3.5\text{-uc SrTiO}_3/1\text{-ML LaO}$ periodic superlattice and insulating behavior for the $3.5\text{-uc SrTiO}_3/1\text{-ML YO}$ periodic superlattice.



6. V. Garcia *et al.*, *Nature* **460**, 81 (2009).
7. H. Kroemer, *Surf. Sci.* **132**, 543 (1983).
8. J. Mannhart, D. G. Schlom, *Science* **327**, 1607 (2010).
9. A. Ohtomo, H. Y. Hwang, *Nature* **427**, 423 (2004).
10. N. Nakagawa, H. Y. Hwang, D. A. Muller, *Nat. Mater.* **5**, 204 (2006).
11. Y. Hotta, T. Susaki, H. Y. Hwang, *Phys. Rev. Lett.* **99**, 236805 (2007).
12. A. Brinkman *et al.*, *Nat. Mater.* **6**, 493 (2007).
13. N. Reyren *et al.*, *Science* **317**, 1196 (2007).
14. Y. Kozuka *et al.*, *Nature* **462**, 487 (2009).
15. S. Thiel, G. Hammerl, A. Schmehl, C. W. Schneider, J. Mannhart, *Science* **313**, 1942 (2006).
16. C. Cen *et al.*, *Nat. Mater.* **7**, 298 (2008).
17. C. Cen, S. Thiel, J. Mannhart, J. Levy, *Science* **323**, 1026 (2009).
18. S. Okamoto, A. J. Millis, *Nature* **428**, 630 (2004).
19. Y. Okimoto, T. Katsufuji, Y. Okada, T. Arima, Y. Tokura, *Phys. Rev. B* **51**, 9581 (1995).
20. Materials and methods are available as supporting material on *Science* Online.
21. H. D. Zhou, J. B. Goodenough, *J. Phys. Condens. Matter* **17**, 7395 (2005).
22. K. Janicka, J. P. Velev, E. Y. Tsymlar, *Phys. Rev. Lett.* **102**, 106803 (2009).
23. M. Imada, A. Fujimori, Y. Tokura, *Rev. Mod. Phys.* **70**, 1039 (1998).
24. F. J. Wong *et al.*, *Phys. Rev. B* **81**, 161101 (2010).
25. H. Ishida, A. Liebsch, *Phys. Rev. B* **77**, 115350 (2008).
26. S. Okatov, A. Poteryaev, A. Lichtenstein, *Europhys. Lett.* **70**, 499 (2005).
27. Z. S. Popovic, S. Satpathy, *Phys. Rev. Lett.* **94**, 176805 (2005).
28. S. Okamoto, A. J. Millis, N. A. Spaldin, *Phys. Rev. Lett.* **97**, 056802 (2006).
29. R. Pentcheva, W. E. Pickett, *Phys. Rev. Lett.* **99**, 016802 (2007).
30. M. Breitschaft *et al.*, *Phys. Rev. B* **81**, 153414 (2010).
31. G. Kotliar *et al.*, *Rev. Mod. Phys.* **78**, 865 (2006).
32. Q. Si, M. J. Rozenberg, G. Kotliar, A. E. Ruckenstein, *Phys. Rev. Lett.* **72**, 2761 (1994).
33. We thank D. G. Schlom and D. A. Muller for fruitful discussions. This work was supported by the National Science Foundation under grant DMR-0906443 and a David and Lucile Packard Fellowship (C.B.E.). The research at University of Nebraska was supported by the Materials Research Science and Engineering Center (NSF grant DMR-0820521), the Nanoelectronics Research Initiative of the Semiconductor Research Corporation, the National Science Foundation (grant

EPS-1010674), and the Nebraska Research Initiative. Work at the University of Michigan was supported by the U.S. Department of Energy (DOE) under grant DE-FG02-07ER46416. We thank the National Center for Electron Microscopy at Lawrence Berkeley National Laboratory for their support under DOE grant DE-AC02-05CH11231 for user facilities. Work at Argonne and use of the Advanced Photon Source were supported by the DOE Office of Science, Office of Basic Energy Sciences, under contract DE-AC02-06CH11357. Work at Brookhaven National Laboratory was sponsored by DOE/BES/MSE and the Center for Functional Nanomaterials under contract DE-AC02-98CH10886. J. Karapetrova's assistance at beamline 33-BM of the Advanced Photon Source is gratefully acknowledged.

Supporting Online Material

www.sciencemag.org/cgi/content/full/331/6019/886/DC1

Materials and Methods

Figs. S1 to S8

Table S1

References

7 October 2010; accepted 19 January 2011

10.1126/science.1198781

Time-Reversed Lasing and Interferometric Control of Absorption

Wenjie Wan, Yidong Chong, Li Ge, Heeso Noh, A. Douglas Stone, Hui Cao*

In the time-reversed counterpart to laser emission, incident coherent optical fields are perfectly absorbed within a resonator that contains a loss medium instead of a gain medium. The incident fields and frequency must coincide with those of the corresponding laser with gain. We demonstrated this effect for two counterpropagating incident fields in a silicon cavity, showing that absorption can be enhanced by two orders of magnitude, the maximum predicted by theory for our experimental setup. In addition, we showed that absorption can be reduced substantially by varying the relative phase of the incident fields. The device, termed a “coherent perfect absorber,” functions as an absorptive interferometer, with potential practical applications in integrated optics.

Time-reversal symmetry is a fundamental symmetry of classical electromagnetic theory and of nonrelativistic quantum mechanics. It implies that if a particular physical process is allowed, then there also exists a “time-reversed process” that is related to the original process by reversing momenta and the direction of certain fields (typically external magnetic fields and internal spins). These symmetry operations are equivalent to changing the sign of the time variable in the dynamical equations, and for steady-state situations they correspond to interchanging incoming and outgoing fields.

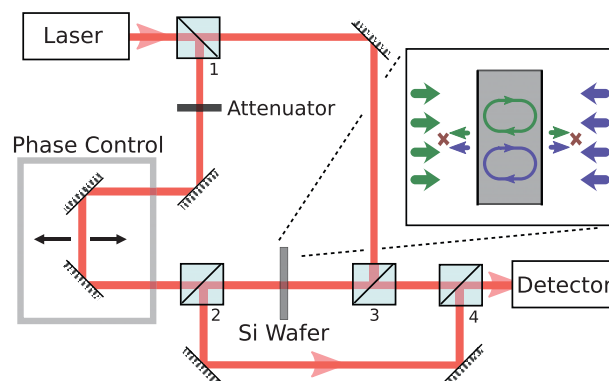
The power of time-reversal symmetry is that it enables exact predictions of the relationship between two processes of arbitrary complexity. A familiar example is spin echo in nuclear magnetic resonance (NMR) (1): A set of precessing spins in a magnetic field fall out of phase because of

slightly different local field environments, quenching the NMR signal. The signal can be restored by imposing an inversion pulse at time T , which has the effect of running the phase of each spin

backward in time, so that after $2T$ they are back in phase, no matter how complicated their local field environment. Time-reversal symmetry is the origin of the well-known weak localization effect (2) in the resistance of metals, the coherent back-scattering peak in the reflection from multiple scattering media (3–5), and the elastic enhancement factor familiar in nuclear scattering (6). Effects due to direct generation of time-reversed waves via special “mirrors” have been extensively studied for sound waves (7–9) and microwave radiation (10).

Recently, several of the authors (11) explored theoretically an exact time-reversal symmetry property of optical systems: the time-reversed analog of laser emission. In the lasing process, a cavity with gain produces outgoing optical fields with a definite frequency and phase relationship, without being illuminated by coherent incoming fields at that frequency. The laser is coupled to an energy source (the pump) that inverts the electron population of the gain medium, causing the onset

Fig. 1. A laser beam from a tunable (800 to 1000 nm) continuous-wave Ti:sapphire source enters a beam splitter (designated 1). The two split beams are directed normally onto opposite sides of a silicon wafer of thickness $\sim 110\ \mu\text{m}$, using a Mach-Zehnder geometry. A phase delay in one of the beam paths controls the relative phase of the two beams. An additional attenuator ensures that the input beams have equal intensities, compensating for imbalances in the beam



splitters and other imperfections. The output beams are rerouted, via beam splitters (designated 2, 3, and 4), into a spectrometer. The inset is a schematic of the CPA mechanism. The incident beams from left and right multiply scatter within the wafer with just the right amplitude and phase so that the total transmitted and reflected beams destructively interfere on both sides, leading to perfect absorption.

Department of Applied Physics, Post Office Box 208284, Yale University, New Haven, CT 06520, USA.

*To whom correspondence should be addressed. E-mail: hui.cao@yale.edu